



Article

Design and Testing of a Non-Contact MEMS Voltage Sensor Based on Single-Crystal Silicon Piezoresistive Effect

Jiachen Li ^{1,2}, Jun Liu ^{1,2}, Chunrong Peng ^{1,2,*}, Xiangming Liu ^{1,2} , Zhengwei Wu ¹ and Fengjie Zheng ¹

¹ State Key Laboratory of Transducer Technology, Aerospace Information Research Institute, Chinese Academy of Sciences, Beijing 100190, China; lijachen19@mails.ucas.ac.cn (J.L.); sushi_1220@163.com (J.L.); liuxiangming18@mails.ucas.ac.cn (X.L.); zwwu@mail.ie.ac.cn (Z.W.); fjiezheng@163.com (F.Z.)

² University of Chinese Academy of Sciences, Beijing 100049, China

* Correspondence: crpeng@mail.ie.ac.cn; Tel.: +86-10-58887590

Abstract: The paper presents a novel non-contact microelectromechanical systems (MEMS) voltage sensor based on the piezoresistive effect of single-crystal silicon. The novelty of the proposed sensor design lies in the implementation of unique single-crystal silicon piezoresistive beams for voltage measurement. The sensitive structure of the sensor produces electrostatic force deformation due to the measured voltage, resulting in the resistance change of single-crystal silicon piezoresistive beams which support a vibrating diaphragm. The voltage can be measured by sensing the resistance change. Moreover, the sensor does not need an additional driving signal and has lower power consumption. The prototype of the sensor was fabricated using an SOI micromachining process. The piezoresistive characteristics of the sensor and the corresponding output response relationship were analyzed through theoretical analysis and finite element simulation. The voltage response characteristics of the sensor were achieved at power frequencies from 50 Hz to 1000 Hz in the paper. The experimental results showed that they were in good agreement with simulations results with the theoretical model and obtained good response characteristics. The sensor has demonstrated that the minimum detectable voltages were 1 V for AC voltages at frequencies from 50 Hz to 300 Hz and 0.5 V for AC voltages at frequencies from 400 Hz to 1000 Hz, respectively. Moreover, the linearities of the sensor were 3.4% and 0.93% in the voltage measurement range of 900–1200 V at the power frequency of 50 Hz and in the voltage measurement range of 400–1200 V at the frequency of 200 Hz, respectively.

Keywords: non-contact voltage measurement; piezoresistive microstructure; low power; MEMS



Citation: Li, J.; Liu, J.; Peng, C.; Liu, X.; Wu, Z.; Zheng, F. Design and Testing of a Non-Contact MEMS Voltage Sensor Based on Single-Crystal Silicon Piezoresistive Effect. *Micromachines* **2022**, *13*, 619. <https://doi.org/10.3390/mi13040619>

Academic Editor: Ha Duong Ngo

Received: 9 March 2022

Accepted: 8 April 2022

Published: 15 April 2022

Publisher's Note: MDPI stays neutral with regard to jurisdictional claims in published maps and institutional affiliations.



Copyright: © 2022 by the authors. Licensee MDPI, Basel, Switzerland. This article is an open access article distributed under the terms and conditions of the Creative Commons Attribution (CC BY) license (<https://creativecommons.org/licenses/by/4.0/>).

1. Introduction

Voltage sensors are widely used in various aspects of power systems, such as transmission, substation, and distribution, to provide accurate and reliable signals for metering, measurement, and control and relay protection devices. Presently, commonly used voltage sensors mainly include contact and non-contact of which contact voltage sensors need to be electrically connected to the power system, which lacks electrical isolation and has security risks, while non-contact voltage sensors cater to the development trend of modern power systems for voltage measurement, with the advantages of more secure and reliable, simple equipment and easy testing [1,2].

In recent years, there have been many reports on non-contact voltage measurement. For optical non-contact voltage sensors, which are mostly based on the electro-optical effect and optical fiber [3–6], although the size of the optical sensor is small and the insulation is good, it is difficult to process optical components, which are high in cost and low in long-term stability and reliability. For non-contact voltage sensors based on the coupling capacitor [7], which realize the non-contact measurement of voltage by connecting the coupling capacitor to the impedance circuit. These sensors are easy to test, safe and reliable but have poor interference immunity and are susceptible to circuitry and

parasitic capacitance. For non-contact voltage sensors based on the measuring principle of the D-dot probe [8], the insulation of the sensor is achieved, and the size of the sensor is smaller; however, the measurement of such sensors is susceptible to environmental influences, and the anti-interference ability and stability need to be improved. For non-contact voltage sensors based on the voltage divider principle, which use the resistive voltage divider, capacitive voltage divider, or resistive-capacitive voltage divider principle to achieve non-contact measurement of voltage, the most significant problem they have is their vulnerability to external ambient temperature and external stray capacitance.

With the development of the microelectromechanical system (MEMS), some non-contact MEMS voltage sensors are reported due to their small size, low power consumption, easy mass production, and integration [9–11]. It is very suitable for large-scale applications such as smart grids and the Internet of things in power systems. These types of sensors have a wide range of structures, but all of them mainly contain electrode-sensitive structures and drive structures. Presently, these sensors are mainly driven by electrostatic drive [12,13], thermal drive [14], and piezoelectric drive [15,16], which leads to high power consumption and complex structure. In summary, there are many shortcomings in the research of non-contact voltage sensors at present, so there is an urgent need to research new miniaturized, low-power, high-performance non-contact voltage sensors.

In this paper, a novel non-contact MEMS voltage sensor based on the piezoresistive effect of a single-crystal silicon structure was proposed. Compared with other voltage sensors, the proposed sensor adopted a unique piezoresistive single-crystal silicon microstructure design, which did not need an additional driving signal and had lower power consumption.

2. Principle and Design

The structure of the MEMS voltage sensor is shown in Figure 1. The sensor consisted of a vibrating diaphragm, supporting beams, and piezoresistive beams. Piezoresistive beams had a straight beam microstructure, and they were connected to a vibrating diaphragm through supporting beams, which was a folded beam structure to reduce the system stiffness. The holes in the membrane of the MEMS device were designed to reduce air damping and facilitate the release of the sensor structure.

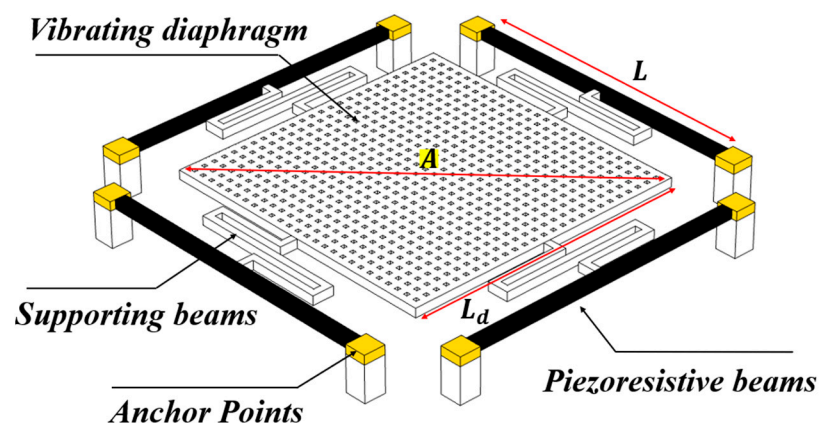


Figure 1. The structure of the sensor.

The operating principle of the MEMS voltage sensor is shown in Figure 2. When the sensor is placed at a distance, d , from the voltage source, the sensor converts the voltage between the voltage source and the diaphragm of the sensor into an electrostatic force. The vibrating diaphragm is displaced vertically because of the electrostatic force, which causes the deflection of the piezoresistive beams. Therefore, the resistance value of the piezoresistive beam changes due to the piezoresistive effect [17]. In this paper, the measured voltage on the voltage source is obtained by measuring the change in resistance value.

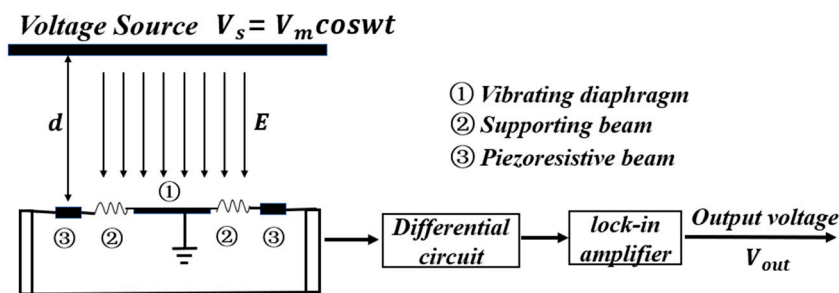


Figure 2. The operating principle of the sensor.

3. Theory and Simulation

The electrostatic force pulling on the diaphragm due to the voltage between the voltage source and the diaphragm of the sensor is given by [18]:

$$F_e = \frac{\epsilon_0 \cdot \epsilon_r \cdot A \cdot V_s^2}{2 \cdot d^2}, \tag{1}$$

where d is the distance separating the diaphragm and the voltage source; A is the surface area of the diaphragm; V_s is the voltage on the nearby voltage source; ϵ_0 and ϵ_r are the vacuum permittivity and the relative permittivity, respectively. When the electrostatic force is loaded at the diaphragm, the concentrated force on the piezoresistive beam is one-fourth of the electrostatic force, which can be analyzed from Figure 1. Therefore, the loading force can be described as:

$$F = \frac{F_e}{4} = \frac{\epsilon_0 \cdot \epsilon_r \cdot A \cdot V_s^2}{8 \cdot d^2}. \tag{2}$$

The piezoresistive beam can be regarded as a doubly clamped beam. A central concentration force is loaded at the piezoresistive beam due to the electrostatic force, which leads to the deflection of the piezoresistive beams. The origin of the piezoresistive conversion can be illustrated by considering the vibration mode shape of the beam, as shown in Figure 3.

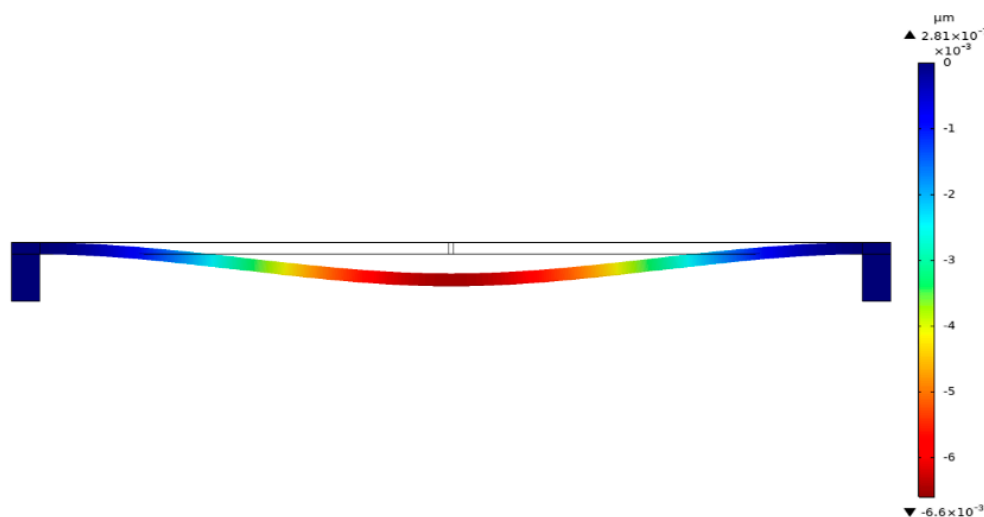


Figure 3. The deflection of a center-loaded doubly clamped beam.

Based on the deflection profile of the doubly clamped beam vibrating in its fundamental mode as described by the Euler beam equation [19], looking at the position x as shown in Figure 4, the displacement function of the beam is written as:

$$w(x) = \frac{FL}{16EI}x^2 - \frac{F}{12EI}x^3, \left(0 \leq x \leq \frac{L}{2}\right), \tag{3}$$

where L is the length of the beam at rest, E is Young’s modulus of the beam, I is the moment of inertia of the beam, and F is the loading force at the middle of the beam as shown in Equation (2). The aggregate axial strain induced by the deflection of the beam is given by [17]:

$$\varepsilon_x = \frac{1}{2L} \int_0^L \left(\frac{\partial w}{\partial x} \right)^2 dx, \tag{4}$$

where L is the length of the beam at rest, and w is the deflection function of the beam, as shown in Equation (3). Therefore, according to Equations (2) and (3), the aggregate axial strain induced by the deflection of the beam, Equation (4) can be written as:

$$\varepsilon_x = a_0 V_s^4, \tag{5}$$

where a_0 is a numerically determined constant. For the piezoresistive beam, its resistance varies, when there is an axial strain. The variation can be written as [20]:

$$\frac{\Delta R}{R} = \pi_l \sigma_l = \pi_l E \varepsilon_x, \tag{6}$$

where ΔR is the resistance variation; R is the original resistance value; π_l is the longitudinal piezoresistive coefficient, which is constant for a fabricated piezoresistive beam; σ_l and ε_x are the axial stress and the axial strain, respectively; E is Young’s modulus of the beam. According to Equations (5) and (6), the resistance variation of the piezoresistive beam can be written as:

$$\frac{\Delta R}{R} = \pi_l E a_0 V_s^4 = c_0 V_s^4, \tag{7}$$

where c_0 is also a constant. It can be seen from Equation (7) that the change in the resistance value of the piezoresistive beam is proportional to the fourth power of the measured voltage. In addition, when the measured voltage is an AC voltage $V_s = V_m \cos(\omega t)$, Equation (7) can be written as:

$$\frac{\Delta R}{R} = C_0 V_m^4 \left(\frac{3}{8} + \cos(2\omega t) + \frac{\cos(4\omega t)}{8} \right). \tag{8}$$

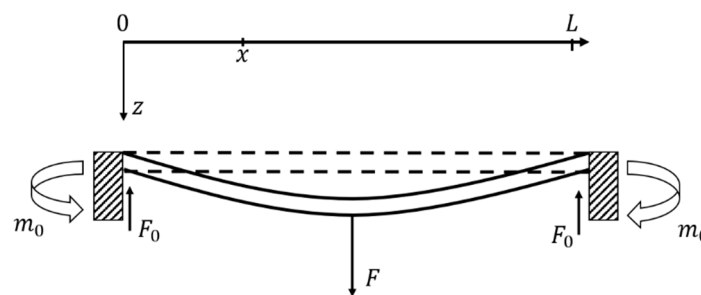


Figure 4. Doubly clamped beam (bridge) and its coordinates.

According to Equation (8), the change in the resistance value of the piezoresistive beam contains a DC component, the second harmonic component, and the fourth harmonic component. In this paper, in order to obtain higher sensitivity and reduce noise, we extracted the signal of the second-harmonic component by filtering to realize the piezoresistive detection, which is proportional to the fourth power of the measured voltage.

To better illustrate the relationship between the resistance change of the piezoresistive beam and the measured voltage, according to Equation (6), the relationship between the axial strain of the piezoresistive beam and the amplitude of the measured voltage was analyzed by using COMSOL finite element simulation software. The simulation model was established as shown in Figure 1, applying the measured voltage above the grounding diaphragm. The boundary conditions were applied to the model, and the simulation results were obtained after meshing and calculation, as shown in Figure 5.

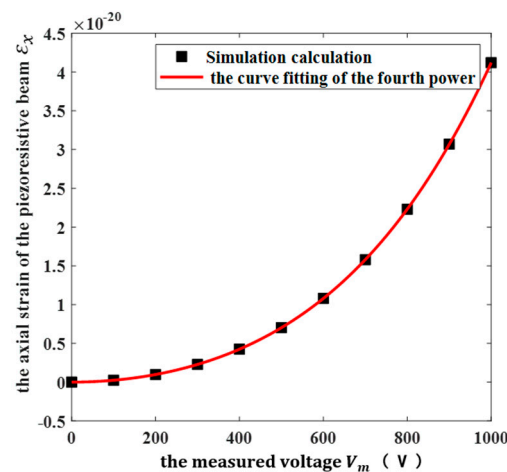
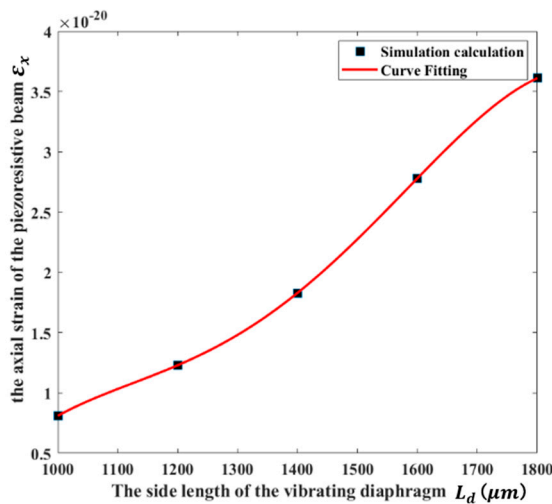


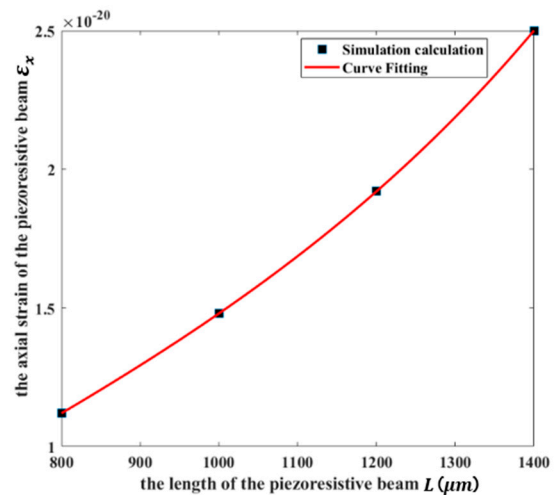
Figure 5. The simulation results between the axial strain of the piezoresistive beam ϵ_x and the amplitude of the measured voltage V_m .

It can be seen from Figure 5 that the axial strain of the piezoresistive beam was proportional to the fourth power of the measured voltage. In addition, according to Equation (6), the change in the resistance value of the piezoresistive beam is linear with the axial strain of the piezoresistive beam; therefore, the change in the resistance value of the piezoresistive beam was proportional to the fourth power of the measured voltage, which was in good agreement with the theoretical model.

To the design of the parameters of the sensor structure, according to Equations (2)–(4) and (7), the vibrating diaphragm area A (the side length of the vibrating diaphragm area L_d) and the length of the piezoresistive beam L have the greatest effects on the resistance variation of the piezoresistive beam. Therefore, Figure 6 shows the finite element simulation results, which is the relationship between the axial strain of the piezoresistive beam and the parameters of the sensor structure.



(a)



(b)

Figure 6. The simulation results between the axial strain of the piezoresistive beam ϵ_x and the parameters of the sensor structure: (a) the side length L_d of the vibrating diaphragm; (b) the length L of the piezoresistive beam.

As can be seen from Figure 6, under the same conditions, the larger the length of the piezoresistive beam L and the side length of the vibrating diaphragm L_d , the greater the axial strain of the piezoresistive beam and the greater the resistance variation of the piezoresistive beam. Therefore, based on the comprehensive consideration of the sensor

structure characteristics analysis, the MEMS manufacturing process rules, and its key dimensional processing constraints, the key parameters of the sensor structure design are shown in Table 1.

Table 1. The key parameters of the sensor.

Key Parameters	Value
the side length of the vibrating diaphragm L_d	2000 μm
the length of the piezoresistive beam L	1750 μm
the width of the piezoresistive beam W_p	10 μm
the thickness of the piezoresistive beam t	25 μm
the width of the supporting beam W_s	10 μm
the single section length of the supporting beam L_s	800 μm

4. Sensor Fabrication

The device was fabricated in a commercial SOIMUMPS process. The SOIMUMPS process is a simple 4-mask-level SOI patterning and etching process. The piezoresistive device was developed as shown in Figure 7.

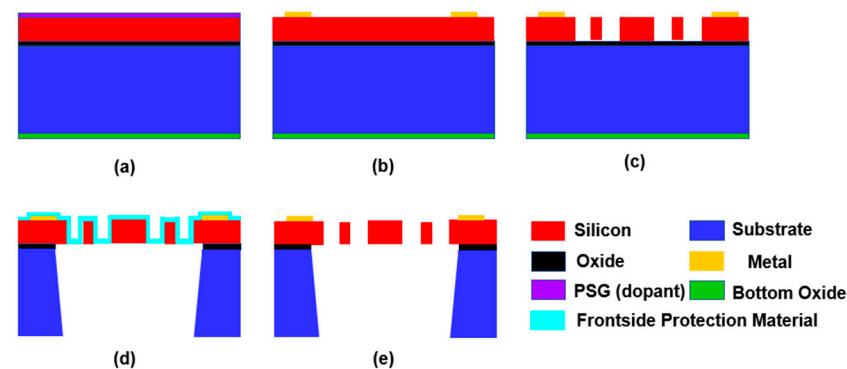


Figure 7. The chip fabrication flow.

The sensor chip was fabricated as below:

- (a) Silicon doping: The top surface of the silicon layer was doped by depositing a phosphor silicate glass (PSG) layer and annealing at 1050 °C for 1 h in argon. The PSG layer was then removed via wet chemical etching;
- (b) Pad metal liftoff: The padded metal was deposited over the device layer by e-beam evaporation;
- (c) Silicon patterning: Silicon was lithographically patterned with a mask and etched using deep reactive ion etching (DRIE);
- (d) Substrate patterning: A frontside protection material was applied to the top surface of the patterned silicon layer. The wafers were then reversed, and the substrate layer was lithographically patterned from the bottom side using a mask. This pattern was then etched into the bottom side oxide layer using reactive ion etching (RIE);
- (e) Protection layer removal: The frontside protection material was then stripped using a dry etching process.

The image of the sensor is shown in Figure 8.

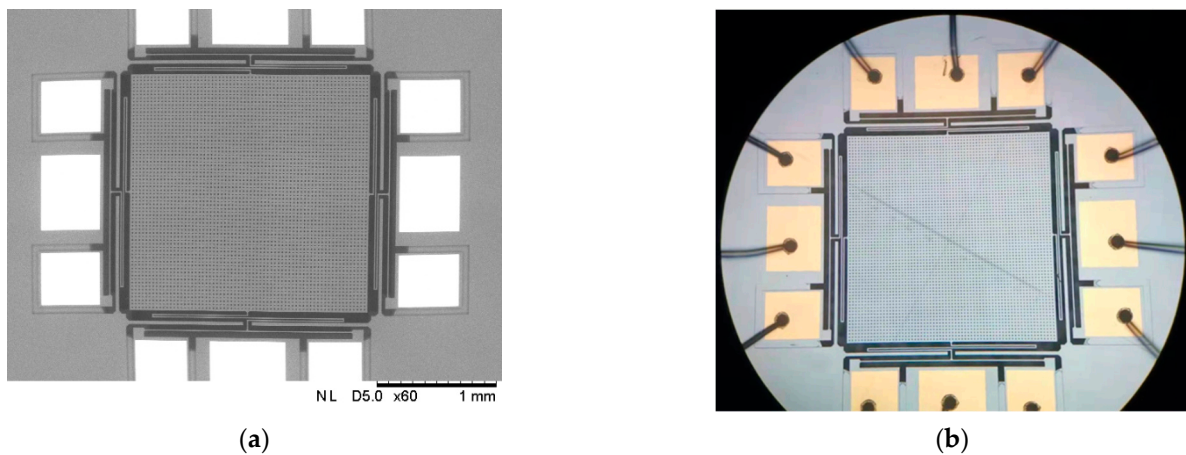


Figure 8. (a) The SEM image of the sensor; (b) the picture of sensor chip under a microscope.

5. Fabrication Experiment Setup

To realize the performance test of the sensor, the test system platform of the sensor was designed. The measurement principle of the sensor is shown in Figure 9. The voltage V_d and $-V_d$ were loaded at both ends of the piezoresistive beam, which caused the vibrating diaphragm grounding. When the sensor was placed at a distance from the measured voltage source, the vibrating diaphragm was displaced vertically due to the electrostatic force, which led to the deflection of the piezoresistive beam. Therefore, the dynamic current in the piezoresistive beam was changed, and the two piezoresistive signals through the isolation capacitor were differentially amplified by AD620. When the resistance value of the piezoresistive beam changes, the dynamic current in the piezoresistive beam can be described as:

$$i \approx \frac{V_d}{R} \left(\frac{\Delta R_r}{R_r} \right), \tag{9}$$

where $R = R_r + 2R_0$; V_d is the supply voltage of the circuit; ΔR_r is the change in the resistance value of the piezoresistive beam; R_r is the original resistance value of the piezoresistive beam; R_0 is the series resistor. Therefore, according to Equation (9), the output voltage at both ends of the piezoresistive beam can be written as:

$$V_{i+} \approx i \cdot \frac{R_r}{2} = \frac{V_d}{R} \left(\frac{\Delta R_r}{R_r} \right) \cdot \frac{R_r}{2}, \tag{10}$$

$$V_{i-} \approx -i \cdot \frac{R_r}{2} = -\frac{V_d}{R} \left(\frac{\Delta R_r}{R_r} \right) \cdot \frac{R_r}{2}. \tag{11}$$

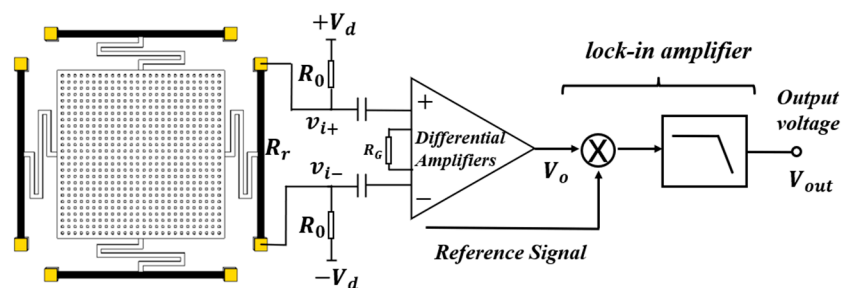


Figure 9. The measurement principle of the sensor.

From the above equations, the output voltage is proportional to the change in resistance of the piezoresistive. According to Equation (8), the output voltage contains a DC component, the second-harmonic component, and the fourth harmonic component. Therefore, a lock-in amplifier was used to measure the second-harmonic component to

obtain higher sensitivity and reduce noise. The amplitude of output voltage is proportional to the fourth power of the measured voltage.

The test system was composed of a power section, the measured voltage power, a lock-in amplifier, a PC, and the measurement circuit, as shown in Figure 10. The power section was used to provide a DC voltage to the circuit, and the voltage V_d was 5 V. The positive terminal of the measured voltage power was connected to a metal pole plate, and the negative terminal was common ground with the circuit. In order to verify the performance of the sensor, the sensor was encapsulated in ceramic and inverted on the metal plate, to which the measured high voltage source was applied. A high-voltage source was a high-precision-power YOKOGAWA 2558A instrument. The high-precision-power YOKOGAWA 2558A was used as the measured voltage power to provide AC voltages in the voltage range of 0–1200 V at the frequency range of 40–1000 Hz. Therefore, the measured voltage caused the deflection of the piezoresistive beam because of the electrostatic force between the vibrating diaphragm and the measured voltage. An HF2LI lock-in amplifier was used to measure the second-harmonic component of the output signals.

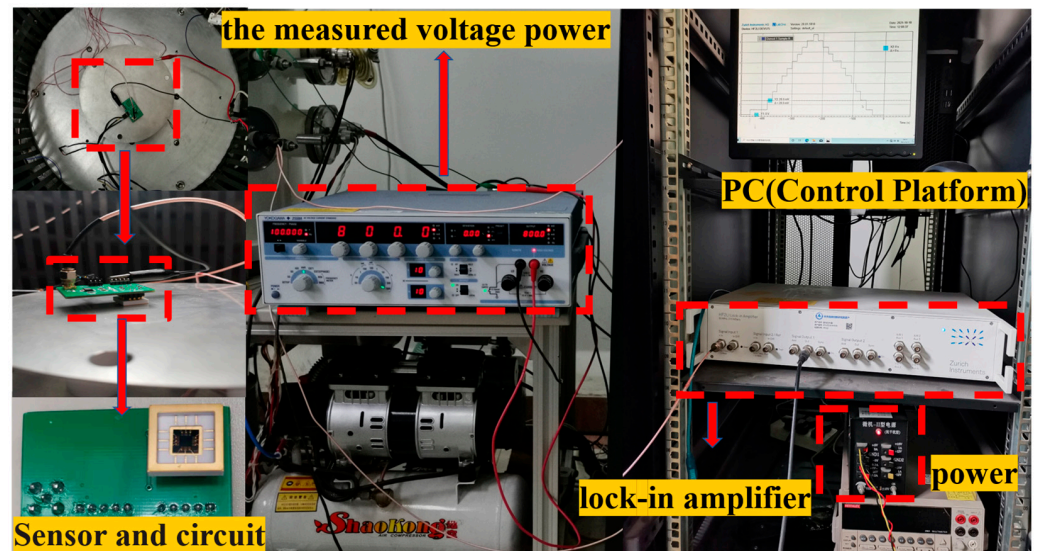


Figure 10. Photo of the experimental setup.

6. Results

6.1. Voltage and Frequency Responses

The voltage response curves of the sensor at different frequencies and the frequency response curves of the sensor at different voltages can be obtained by changing the frequency and amplitude of the measured voltage power, as shown in Figure 11.

It can be seen from Figure 11a that there was a non-linear relationship between the sensor output voltage and the measured voltage, and the sensor output voltage increased with the measured voltage. To explain the relationship between the output voltage and the measured voltage more clearly, the voltage response curves of the sensor at the frequencies of 50 Hz, 200 Hz, 500 Hz, and 1000 Hz are curve-fitted, as shown in Figure 12.

It can be concluded from Figure 12 that the output voltage was proportional to the fourth power of the measured voltage, which is in good agreement with the theoretical model. In addition, there was also a non-linear relationship between the sensor output voltage and the frequency of the measured voltage, as shown in Figure 11b, and the sensor output voltage increased with the frequency of the measured voltage in the measurement frequency range.

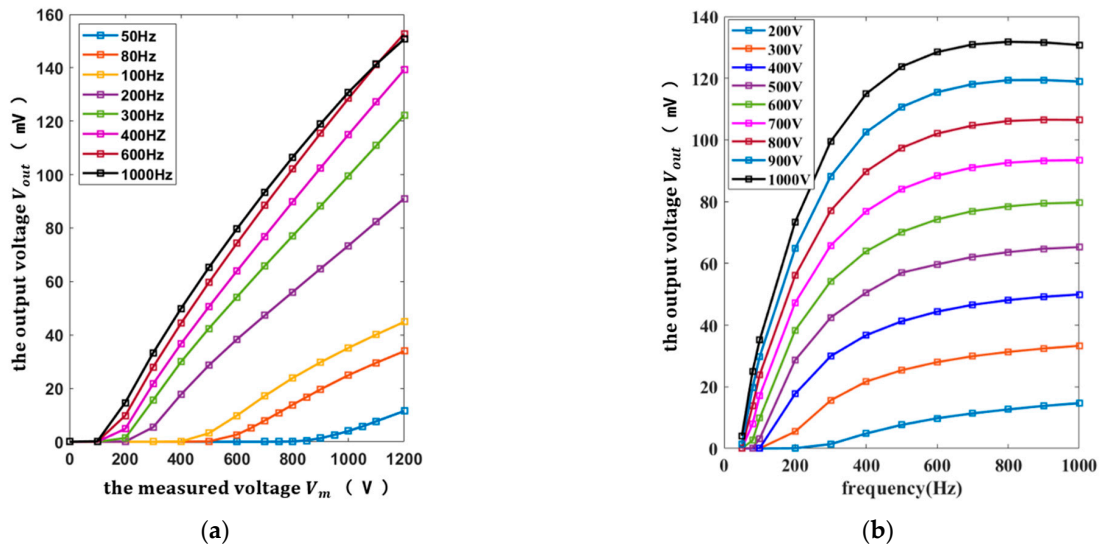


Figure 11. The voltage response curves of the sensor at different frequencies and the frequency response curves of the sensor at different voltages: (a) the voltage response curve of the sensor; (b) the frequency response curve of the sensor.

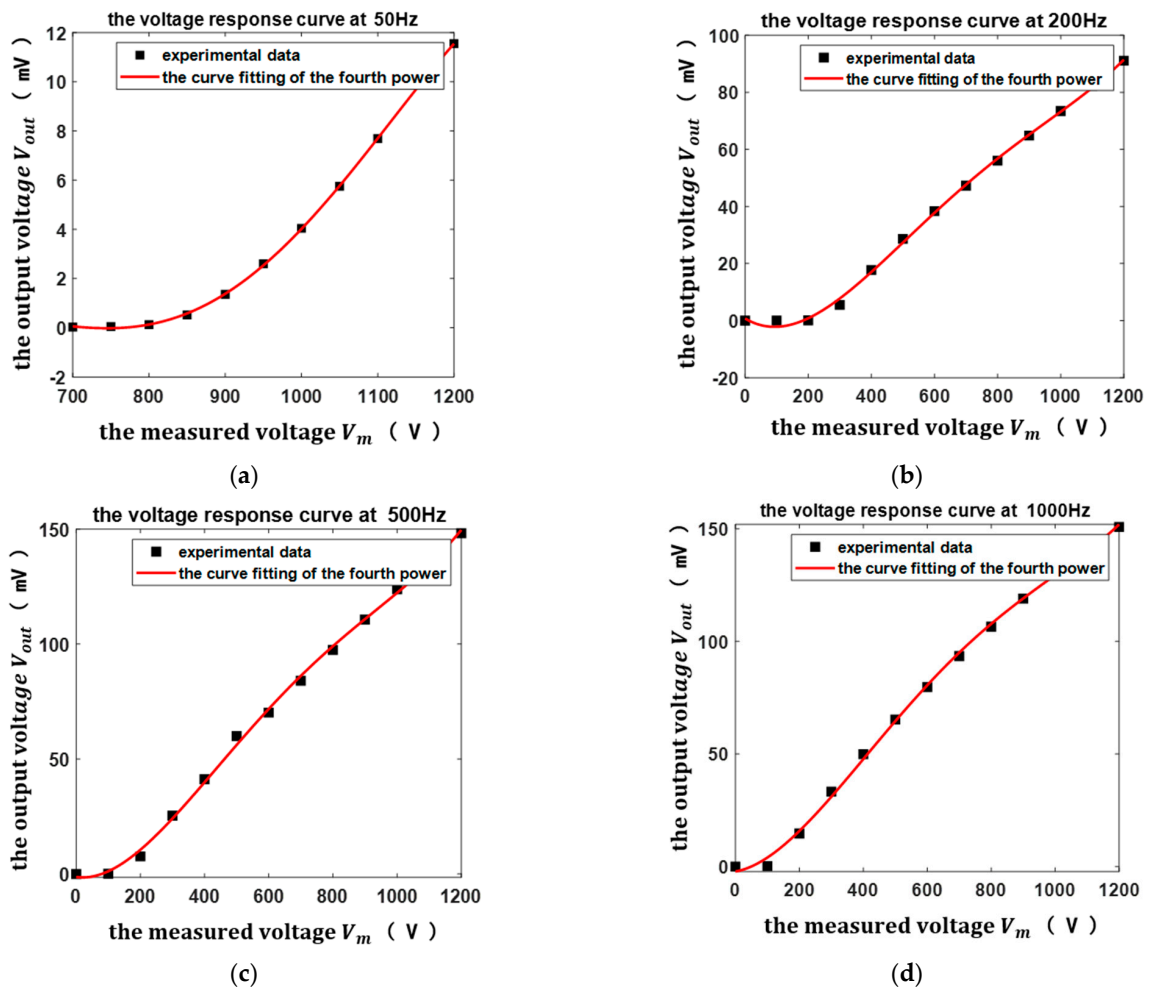


Figure 12. The voltage response curves of the sensor curve-fitted at the frequencies: (a) 50 Hz; (b) 200 Hz; (c) 500 Hz; (d) 1000 Hz.

6.2. Linearity and Sensitivity

According to Figure 11, the output voltage was linearly proportional to the voltage measurement range of 900–1200 V at the frequency of 50 Hz, the voltage measurement range of 400–1200 V at the frequency of 200 Hz, the voltage measurement range of 300–1200 V at the frequency of 500 Hz, and the voltage measurement range of 200–1200 V at the frequency of 1000 Hz separately, as shown in Figure 13.

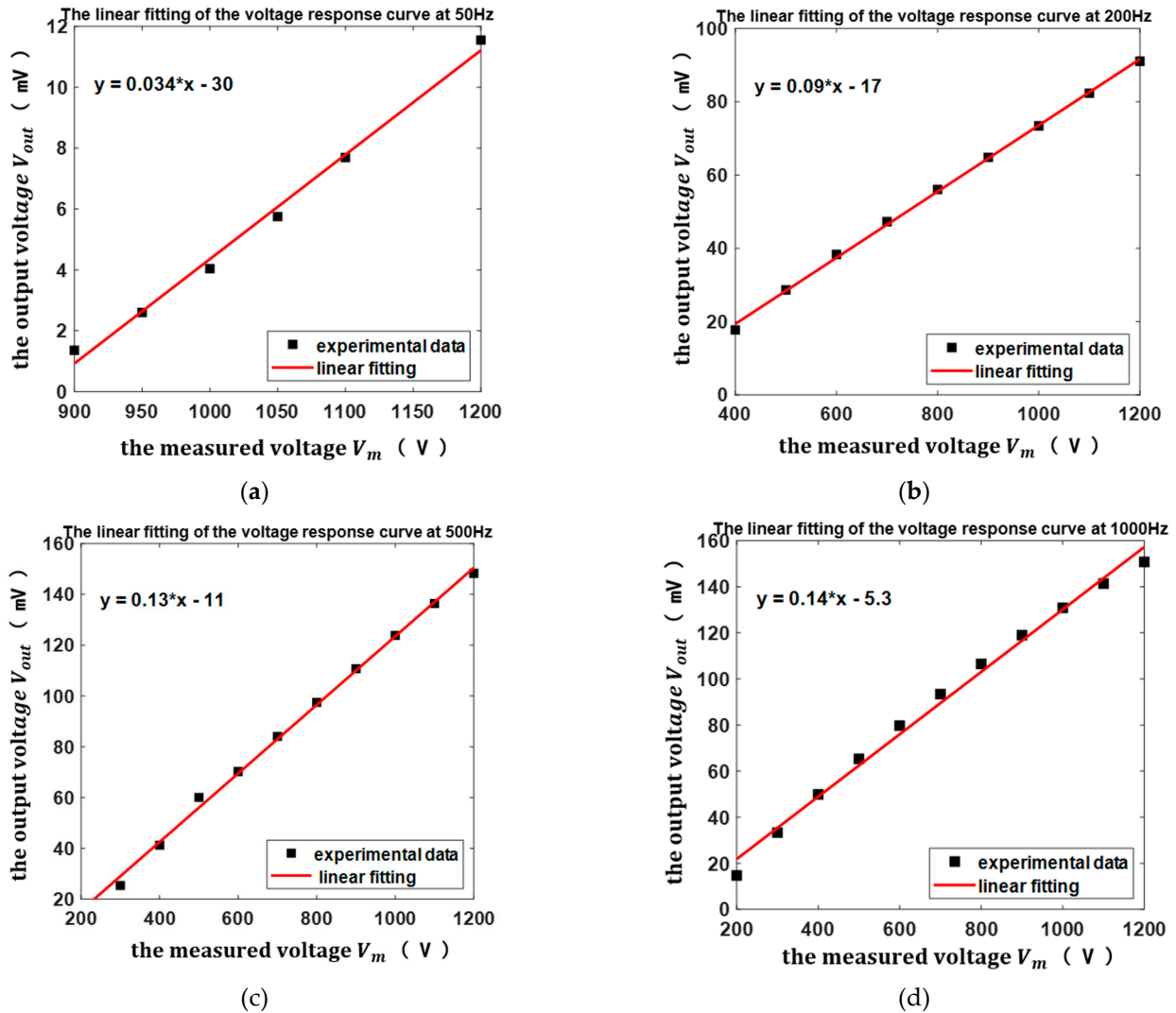


Figure 13. The linear fittings of the sensor voltage response curves at frequencies: (a) 50 Hz; (b) 200 Hz; (c) 500 Hz; (d) 1000 Hz.

According to Figure 13, the data showed a good linear relationship between the sensor output voltage and the measured voltage. The linearity and sensitivity values at different frequencies can be calculated as shown in Table 2. Moreover, the lowest voltage amplitudes that could be accurately measured were 1 V from 50 Hz to 300 Hz and 0.5 V from 400 Hz to 1000 Hz, as shown in Table 2.

Figure 13 and Table 2 show that the sensor had a good linear response to the voltage amplitude and can be used to measure AC voltages at power frequencies from 50 Hz to 1000 Hz in this paper.

Table 2. The linearity, sensitivity, and resolution of the sensor.

Frequency (Hz)	Linearity	Sensitivity (mV/V)	Resolution (V)
50	3.4%	0.034	1
200	0.93%	0.09	1
500	1.62%	0.13	0.5
1000	3.87%	0.14	0.5

Compared with other MEMS voltage sensors [21–23] as shown in Table 3, the voltage sensor proposed in this paper did not need any driving structures and any additional driving signals, which realized the low-power measurement of the sensor. Moreover, the test circuit of the sensor was simple, and the static power consumption of the circuit depended on the series resistor R_0 . In addition, when the series resistor R_0 was 100 k Ω , the sensor consumption including the test circuit was on the order of milliwatts or lower.

Table 3. The comparison with other microelectromechanic systems (MEMS) voltage sensors.

Source	Driving Structure	Driving Signals
[21]	thermal drive	a driving voltage of 75 mV (vacuum environment)
[22]	electrostatic drive	a DC bias voltage of 20 V and an AC voltage amplitude of 1 V
[23]	electrostatic drive	a DC bias voltage of 8 V and an AC voltage of 10 V (peak-to-peak)
this work	no driving structure	no driving voltage

7. Conclusions

In this paper, a novel MEMS non-contact voltage sensor based on the piezoresistive effect of a single-crystal silicon structure was demonstrated. The sensor achieved low power consumption measurement without any driving structure and any additional drive signals. In addition, the power dissipation of the test circuit was on the order of milliwatts or lower. The entire single-crystal silicon beam was used as a piezoresistive element to improve the sensitivity of the sensor and simplify the process. Based on the SOI MEMS process, the device prototype was fabricated. Experimental tests showed that the sensor output response characteristics were consistent with theoretical analysis and the sensor has obtained fine linearity and sensitivity. The lowest voltage amplitudes experimentally measured were 1 V at frequencies from 50 Hz to 300 Hz and 0.5 V at frequencies from 400 Hz to 1000 Hz. The linearities of the sensor were 3.4% and 0.93% in the voltage measurement range of 900–1200 V at the power frequency of 50 Hz and the voltage measurement range of 400–1200 V at the power frequency of 200 Hz, respectively. In the future, we will further carry out application verification for practical application scenarios, such as power transmission, transformation, and distribution, and study the anti-interference characteristics of the sensor. In addition, for low-voltage measurements, such as below 220 V, the sensor will be further optimized to improve the measurement sensitivity.

Author Contributions: Conceptualization, J.L. (Jiachen Li), J.L. (Jun Liu) and X.L.; Data curation, J.L. (Jiachen Li); Formal analysis, J.L. (Jiachen Li); Funding acquisition, C.P.; Investigation, J.L. (Jiachen Li) and J.L. (Jun Liu); Methodology, J.L. (Jiachen Li), J.L. (Jun Liu) and X.L.; Project administration, C.P.; Resources, J.L. (Jiachen Li) and C.P.; Software, J.L. (Jiachen Li) and X.L.; Supervision, J.L. (Jiachen Li), Z.W. and F.Z.; Validation, J.L. (Jiachen Li); Visualization, J.L. (Jiachen Li); Writing—original draft, J.L. (Jiachen Li); Writing—review & editing, C.P., Z.W. and F.Z. All authors have read and agreed to the published version of the manuscript.

Funding: This study was funded by the National Natural Science Foundation of China (grant numbers: 62031025 and 61971398) and the Scientific Instrument Developing Project of the Chinese Academy of Sciences (grant numbers: YJKYYQ20200026 and GJJSTD20210004).

Institutional Review Board Statement: Not applicable.

Informed Consent Statement: Not applicable.

Data Availability Statement: Not applicable.

Acknowledgments: This work was partly carried out at the State Key Laboratory of Transducer Technology. The authors would like to thank the comrades, who gave us valuable suggestions.

Conflicts of Interest: The authors declare no conflict of interest.

References

1. Zhang, X.; Yue, B.; Huang, J.; Ruan, Y.; Zhang, P. Research on Non-contact Voltage Measurement Technology. In Proceedings of the 2019 IEEE 2nd International Conference on Automation, Electronics and Electrical Engineering (AUTEEE), Shenyang, China, 22–24 November 2019; pp. 534–537.
2. Kang, S.; Yang, S.; Kim, H. Non-intrusive voltage measurement of ac power lines for smart grid system based on electric field energy harvesting. *Electron. Lett.* **2016**, *53*, 181–183. [[CrossRef](#)]
3. Pustelny, T.P. Electroluminescent optical fiber sensor for detection of a high intensity electric field. *Photonics Lett. Pol.* **2020**, *12*, 19–21. [[CrossRef](#)]
4. Sharma, I.; Chaudhuri, P.R. A new approach to sensing low electric field using optical fibers' beam-deflection configuration with BiFe_{0.9}Co_{0.1}O₃ nanoparticles as probe and determination of polarisation. *Opt. Fiber Technol.* **2021**, *62*, 102472. [[CrossRef](#)]
5. Shinagawa, M. Sensitive electro-optic sensor using KTa_{1-x}Nb_xO₃ crystal. *Sens. Actuators A Phys.* **2013**, *192*, 42–48. [[CrossRef](#)]
6. Lyu, F.; Ding, H.; Han, C. Electric-field sensor based on propylene carbonate cladding microfiber sagnac loop interferometer. *IEEE Photonics Technol. Lett.* **2018**, *1*. [[CrossRef](#)]
7. Reza, M.; Rahman, H.A. Non-Invasive Voltage Measurement Technique for Low Voltage AC Lines. In Proceedings of the 2021 IEEE 4th International Conference on Electronics Technology (ICET), Chengdu, China, 7–10 May 2021; pp. 143–148.
8. Wang, D.; Li, P.; Wen, Y. Design and modeling of magnetically driven electric-field sensor for non-contact DC voltage measurement in electric power systems. *Rev. Sci. Instrum.* **2016**, *87*, 123–212. [[CrossRef](#)] [[PubMed](#)]
9. Kainz, A.; Steiner, H.; Schalko, J. Distortion-free measurement of electric field strength with a MEMS sensor. *Nat. Electron.* **2018**, *1*, 68–73. [[CrossRef](#)] [[PubMed](#)]
10. Yang, P.; Bo, C.; Wen, X.; Peng, C.; Hao, Y. A novel MEMS chip-based atmospheric electric field sensor for lightning hazard warning applications. In Proceedings of the 2015 IEEE SENSORS, Busan, Korea, 1–4 November 2015; pp. 1–4.
11. Ma, Q.; Huang, K.; Yu, Z. A MEMS-Based Electric Field Sensor for Measurement of High-Voltage DC Synthetic Fields in Air. *IEEE Sens. J.* **2017**, *23*, 7866–7876. [[CrossRef](#)]
12. Peng, C. Design and testing of a micromechanical resonant electrostatic field sensor. *J. Micromech. Microeng.* **2006**, *16*, 914–919. [[CrossRef](#)]
13. Yang, P. Design, fabrication and application of an SOI-based resonant electric field microsensor with coplanar comb-shaped electrodes. *J. Micromech. Microeng.* **2013**, *23*, 055002. [[CrossRef](#)]
14. Bahreyni, B. Analysis and Design of a Micromachined Electric-Field Sensor. *J. Microelectromechanical Syst.* **2008**, *17*, 31–36. [[CrossRef](#)]
15. Kobayashi, T. Microelectromechanical Systems-Based Electrostatic Field Sensor Using Pb(Zr,Ti)O₃ Thin Films. *Jpn. J. Appl. Phys.* **2014**, *47*, 7533–7536. [[CrossRef](#)]
16. Lei, H.; Xia, S.; Chu, Z. An Electric Field Microsensor with Mutual Shielding Electrodes. *Micromachines* **2021**, *12*, 360. [[CrossRef](#)] [[PubMed](#)]
17. Senturia, S. *Microsystem Design*; Kluwer: Boston, MA, USA, 2001.
18. Chen, T. Micromachined ac/dc electric field sensor with modulated sensitivity. *Sens. Actuators A Phys.* **2016**, *245*, 76–84. [[CrossRef](#)]
19. Bao, M. *Chapter 2 Basic Mechanics of Beam and Diaphragm Structures*; Elsevier: Amsterdam, The Netherlands, 2000; pp. 23–88.
20. Lee, L. *Principles of Microelectromechanical Systems*; Springer: Dordrecht, The Netherlands, 2011.
21. Wijeweera, G.; Bahreyni, B.; Shafai, C. Micromachined Electric-Field Sensor to Measure AC and DC Fields in Power Systems. *IEEE Trans. Power Deliv.* **2009**, *24*, 988–995. [[CrossRef](#)]
22. Yang, P.; Wen, X.; Yao, L.; Chu, Z.; Peng, C. A non-intrusive voltage measurement scheme based on MEMS electric field sensors: Theoretical analysis and experimental verification of AC power lines. *Rev. Sci. Instrum.* **2021**, *92*, 065002. [[CrossRef](#)] [[PubMed](#)]
23. Mm, A.; Km, B.; App, A. MEMS-based non-contact voltage sensor with multi-mode resonance shutter. *Sens. Actuators A Phys.* **2019**, *294*, 25–36.